Tunable valence tautomerism in lanthanide-organic alloys

Maja A. Dunstan[1]✉, Anna S. Manvell[1], Nathan Yutronkie[2], Frédéric Aribot[1], Jesper Bendix[3], Andrei Rogalev[2] & Kasper S. Pedersen[1]✉

[1] Department of Chemistry, Technical University of Denmark, DK-2800 Kgs. Lyngby (Denmark)

[2] European Synchrotron Radiation Facility, BP 220, 38043 Grenoble Cedex 9 (France)

[3] Department of Chemistry, University of Copenhagen, DK-2300 Copenhagen (Denmark)

✉ e-mail: kastp@kemi.dtu.dk (K.S.P.), majdu@kemi.dtu.dk (M.A.D.)

The electronic structures of the lanthanide (*Ln*) ions are inimitable and key to advanced materials and technologies. The trivalent ions are ubiquitous and dwarf the use of di- and tetra-valent analogues, which, however, possess vastly different optical and magnetic properties. Hence, alteration of the valence electron count by external stimuli would lead to dramatic changes in materials properties. Compounds exhibiting a temperature-induced, complete *Ln*(III) ⇄ *Ln*(II) switch, referred to as a valence tautomeric (VT) transition, are virtually absent. Herein, we present an abrupt and hysteretic VT transition in a lanthanide-based coordination polymer, $SmI_2(pyrazine)_3$, driven by the interconversion of closed-shell Sm(II)-pyrazine(0) and paramagnetic Sm(III)-pyrazine(•–) redox pairs. Alloying $SmI_2(pyrazine)_3$ with Yb(II) yields isomorphous $Sm_{1-x}Yb_xI_2(pyrazine)_3$ solid solutions with VT transition critical temperatures ranging widely from 200 K to ~50 K at ambient pressure. These findings demonstrate a simple strategy to realize thermally switchable magnetic materials with chemically tunable transition temperatures.

The lanthanide (4*f*) elements receive ever-increasing attention as fundamental components of advanced materials owing to their unique electronic structures.[1] While the trivalent ions are omnipresent for the entire *Ln* series, the divalent and tetravalent ions,[2,3] and mixed-valence systems,[4] host vastly different electronic structures and properties. Given the dramatic changes in physical and chemical properties of a lanthanide-based compound following a change in the formal valence state, materials with an intrinsic possibility for switching oxidation state have been intensively investigated.[5] Whilst several inorganic solids and molecular complexes hosting intermediate lanthanide valence have been reported,[6] compounds demonstrating a change in oxidation state by external stimuli remain exceedingly rare. In inorganic solids, prominent examples include pressure-actuated VT transitions tied to emergence of superconductivity in elemental Eu and Yb,[7,8] and semiconductor-to-semimetal transitions in Sm monochalcogenides.[9] In SmS, for instance, the application of a 6.5 kbar pressure leads to a discontinuous (first-order) 'black-golden' phase transition attributed to the promotion of one electron from the $4f^6$ configuration to the conduction band, formally corresponding to an idealized Sm(II)-to-Sm(III) VT transition.[10,11] However, the full +III oxidation state is only attained at even higher pressures in the metallic, correlated heavy fermion phase.[12,13] In other systems, such as SmB_6, the energies of the +II and +III states are comparable and lead to strongly correlated Kondo insulators and new paradigms for mixed valency.[14,15] Despite this energy proximity, temperature-induced VT transitions are, in general, extremely rare and have only been observed in metallic, ternary phases for undoped materials.[16] In materials with molecular constituents, a gradual VT transition from a valence of +2.3 to +2 was found to drive a negative thermal expansion in the fulleride $Sm_{2.75}C_{60}$.[17] In insulators, hosting well-defined metal oxidation states, lanthanide VT is virtually absent. This contrasts with the 3*d* transition metal compounds for which VT transitions have been well-established for more than forty years.[18,19,20] A singular example of a lanthanide-based complex exhibits a temperature-induced VT transition.[21,22] For a single crystal of one of the polymorphs of the dinuclear [Yb(dpp-bian)(dme)(μ-Cl)]$_2$ (dme = 1,2-dimethoxyethane, dpp-bian = 1,2-bis[(2,6-di-isopropylphenyl)imino]acenaphthene), one of the Yb centers experiences a reversible, abrupt

increase in the magnetic moment around 150 K, attributed to a Yb(II)-to-Yb(III) VT transition. The complete absence of the phenomenon in either of the two highly similar polymorphs could suggest an extreme sensitivity of the VT transition in molecule-based lanthanide compounds towards minuscule structural changes. This, in turn, could discourage further exploitation of this property. Herein, we report a quantitative and reversible VT transition in a bulk Sm-based coordination polymer, $SmI_2(pyz)_3$ (pyz = pyrazine), and demonstrate the tunability of the VT transition event by chemical doping. The interest in pyrazine as a redox-active bridging ligand has flourished due to the recent observation of high-temperature ferrimagnetism with large coercivity,[23,24,25,26] and metallic conductivity[27] in two-dimensional, pyrazine-based coordination polymers based on 3*d* transition elements. For instance, the reaction of $CrCl_2$ and pyz leads to a complete metal–ligand redox reaction and the formation of $Cr^{III}Cl_2(pyz)(pyz^{\bullet-})$.[23] Here, the strong magnetic superexchange interactions and the semiconducting properties are intimately linked to the energetic proximity of metal and linker frontier orbitals and their hybridization.[23] A similar matching of orbital energies has hitherto been unsuccessful for any lanthanide-based coordination polymer. We recently reported on the use of *trans*-$\{LnI_2\}^{0/+}$ units as structure-directing motifs in 2D coordination polymers.[28,29] The reaction between EuI_2 and pyz in solution led to the isolation of 2D-polymeric $EuI_2(pyz)_{5/2}$.[30] Despite the resemblance of the Eu(III)/Eu(II) (E^o = –0.35 V) and the Cr(III)/Cr(II) (E^o = –0.42 V) potentials,[31] no indications of electron transfer from Eu(II) to the pyz scaffold were observed, emphasizing the need for larger reduction potentials—for instance those found for the Yb(III)/Yb(II) (E^o = –1.1 V) and Sm(III)/Sm(II) (E^o = –1.5 V) couples. In organic synthesis, samarium diiodide ("Kagan's reagent") in tetrahydrofuran has proven to be an exceedingly useful single-electron transfer agent towards a wide variety of substrates,[32] emphasizing that conditions for realizing reversible Sm(II)–ligand electron transfer events in solid materials may be possible to achieve.

Results & discussion

Structural analysis

Addition of a warm acetonitrile solution of LnI_2 (*Ln* = Sm, Yb) to a melt of pyz leads to the immediate formation of a crystalline compound, hereafter denoted **Sm** and **Yb**. Room-temperature powder X-ray diffraction data (Supplementary Fig. 1) suggest that **Sm** and **Yb** are isostructural, with minor unit cell differences as expected from the lanthanide contraction. Single-crystal X-ray diffraction analysis at 230 K reveals **Sm** to be $SmI_2(pyz)_3$, which exhibits a 1D "ladder"-type structure along *b* composing of edge-sharing $\{Sm_3I_6(\mu\text{-pyz})_3\}$ triangles, decorated by pendant pyz ligands (Fig. 1). Cooling **Sm** to 170 K leads to a cell volume reduction of 5.9%, without any change in crystallographic symmetry. The structural differences between the 170 and 230 K phases are

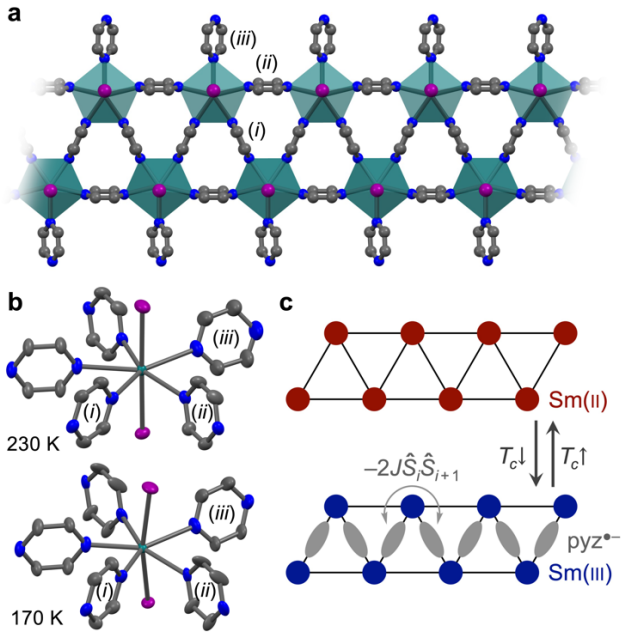

Fig. 1 | Single-crystal X-ray diffraction structure of $SmI_2(pyz)_3$. Fragment of the infinite, triangular ladder structure running along the crystallographic *b* direction (*T* = 170 K), highlighting the approximate D_{5h} coordination geometry of the Sm centers (**a**). Teal, Sm; purple, I; blue, N; grey, C. H atoms and positional disorder of pyz (*iii*) have been omitted for clarity. **b**, Thermal ellipsoid plots (50% probability level) of the $\{SmI_2(pyz)_5\}$ units of **Sm** at *T* = 230 K (top) and *T* = 170 K (bottom). **c**, Schematic representation of the temperature-induced VT transition, the localization of the $pyz^{\bullet-}$, and the formation of 1D zig-zag spin-chains.

evidenced by the metrics of the Sm coordination spheres. The 170 K Sm—I bonds (3.085(2), 3.073(1) Å) are significantly shorter (~4%) than those determined at 230 K (3.1933(9), 3.1977(8) Å), and close to the average Yb–I bond length (3.09 Å, 120 K; Supplementary Fig. 2). For comparison, the structurally related ~D_{5h}-symmetric $Ln^{II}I_2(CH_3CN)_5$ (*Ln* = Sm, Yb) complexes exhibiting Sm—I and Yb—I bond lengths of 3.24 Å and 3.12 Å (at 120 K), respectively.[33] Temperature-dependent powder X-ray diffraction data for **Sm** (Supplementary Fig. 3–5) evidence an abrupt shift of the reflections at ~190 K during cooling and a full reversibility upon heating at ~205 K. These combined observations indicate the occurrence of a reversible, first-order phase transition coupled to a Sm(III) ⇄ Sm(II) VT transition. The electron transfer implies a reduction of the pyz scaffold, as found in the 3*d* congeners.[23,27] The crystallographically unique pyz ligands are denoted by (*i*), (*ii*), and (*iii*) (*cf.* Fig. 1ab). The Sm—N bond lengths (Å) at 230 K (170 K) are 2.753(4) (2.42(1)), 2.724(4) (2.62(1)), and 2.702(7) (2.69(2)) for (*i*), (*ii*), and (*iii*), respectively. While the minor 4% and 0.5% decrease of the Sm—N distances for (*ii*) and (*iii*) are as expected for an increase in oxidation state from Sm(II) to Sm(III), the 12% reduction for (*i*) suggests the localization of the radical spins on that pyz ligand. Further justification is provided by the N—C and C—C bond lengths of (*i*), for which the N—C

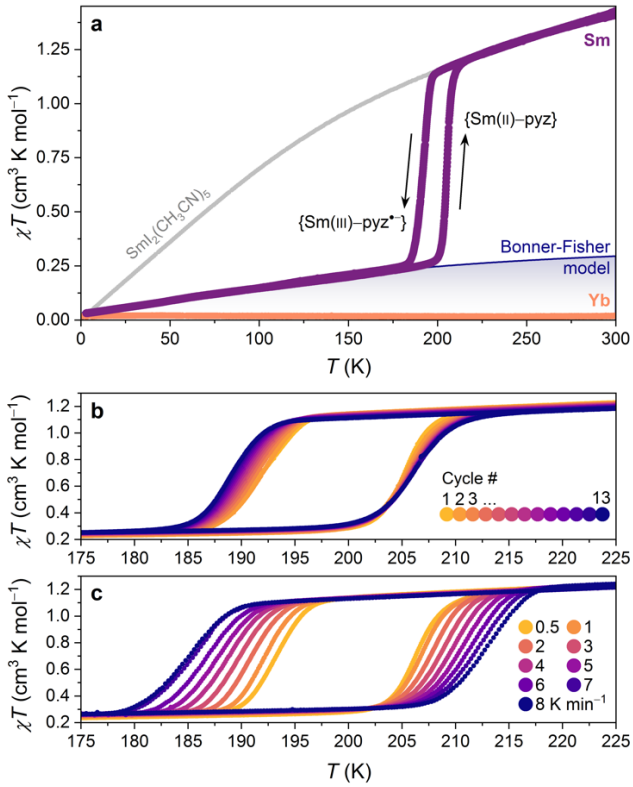

Fig. 2 | Magnetic properties of $SmI_2(pyz)_3$. a, Temperature dependence of the magnetic susceptibility-temperature product, χT ($\chi = M/\mu_0 H$; $\mu_0 H$ = 1.0 T), of **Sm** obtained under heating and cooling (0.25 K min^{-1} between 170 and 230 K. 1 K min^{-1} elsewhere). The χT product for **Yb** (diamagnetic) and $SmI_2(CH_3CN)_5$ (reproduced from ref. 33) are shown for comparison. The solid blue line represents the Bonner-Fisher chain-model calculation as described in the main text. **b**, Successive cooling-heating cycles (0.25 K min^{-1}) of the χT product of **Sm** around the VT transition. **c**, Sweep rate-dependence of the cooling-heating cycles of **Sm** at the indicated rates.

and C—C bonds elongate by 1.5% and contract by 1.3%, respectively, as expected for a one electron reduction.[34] Finally, the I—Sm—I angle changes from 178.83(3)° (230 K) to 167.13(4)° (170 K), where the I^- ligands bend away from the two (*i*) pyz coordinated to each Sm center (Fig. 1b). This structural analysis implies the formation of 1D zig-zag chains of $pyz^{\bullet-}$ (*i*) following the Sm(II) ⇄ Sm(III) conversion (Fig. 1c).

Magnetic properties & X-ray spectroscopy

The magnetic susceptibility-temperature product, χT, of **Yb** is vanishingly small in the full temperature window (3–300 K), reflecting the closed-shell electronic configuration of Yb(II) ($4f^{14}$) and pyz. The room-temperature χT product for **Sm** amounts to 1.41 cm^3 K mol^{-1}. For Sm(II) ($4f^6$), the non-magnetic $^7F_0$ ground state is separated from the excited $^7F_1$ state by only ~400 K, leading to a sizable room-temperature χT product, which for **Sm** coincides with that of the Sm(II) complex, $SmI_2(CH_3CN)_5$ (Fig. 2a). Lowering the temperature leads to a steady decrease in the χT product, which, near $T_c\downarrow$ = 192 K, experiences a precipitous drop leading to a χT product of 0.25 cm^3 K mol^{-1} at 180 K.[35] Reheating the sample leads to a fully reversible, hysteretic behavior of the χT product with $T_c\uparrow$ = 206 K. This unusual behavior may be interpreted as a manifestation of the Sm(II) ⇄ Sm(III) interconversion, with a concurrent redox event happening in the pyz scaffold. This tautomerism is confirmed by X-ray absorption near-edge structure (XANES) spectroscopy around the Sm L_3 absorption edge of **Sm** (Fig. 3). At room temperature, the intense "white line", corresponding to dipole-allowed $2p \rightarrow 5d$, $6s$ transitions, has a maximum at a photon energy of 6715 eV, commensurate with an oxidation state assignment of Sm(II).[36] Cooling to 44 K leads to a shift of the white line of 8 eV towards higher photon energy, characteristic of the $4f^5$ configuration, i.e. an increase in effective Sm oxidation state at low temperature. This behaviour parallels the shift observed for the pressure-induced VT transition in SmS.[37] The photon energy of the weak pre-edge shoulder in the spectrum recorded at 44 K coincides with the energy of the expected quadrupolar $2p \rightarrow 4f$ transitions of Sm(III) and, thus cannot be unambiguously assigned to an incomplete VT transition.[38] For a quantitative conversion, the χT product should reflect a Sm(III) and a spin-½ radical anion. Sm(III) ($4f^5$) possesses a weakly magnetic $^6H_{5/2}$ (g_J = 2/7) ground state with a Curie constant of just 0.09 cm^3 K mol^{-1}, while a radical spin-½ contributes by 0.37 cm^3 K mol^{-1} (for g = 2). The 180 K χT product of 0.25 cm^3 K mol^{-1}, that decreases steadily to ~0.03 cm^3 K mol^{-1} at 3 K, suggests the presence of significant spin-spin interactions in **Sm**. The magnetic moment at 3 K and 9 T amounts to only 0.19 μ_B, which may primarily originate from Sm(III) (Supplementary Fig. 6). Following the structural discussion, the spin-structure of **Sm** below T_c may be described as a one-dimensional chain of $pyz^{\bullet-}$ radicals linked by Sm(III) ions (*cf.* Fig. 1c). In a first approximation, the χT product data may be modeled as a one-dimensional chain of spin-½ moments with the small Sm(III) magnetic moment incorporated as a Curie law-contribution.[39] Simulation of the χT product data below T_c using the Bonner-Fisher model for spin-½ chains afforded J/hc = −76 cm^{-1} ($-2JS_iS_{i+1}$ Hamiltonian definition).[40] Such strong magnetic superexchange interaction of radical spins across a lanthanide ion is unprecedented. Alternatively, given the close proximity of the $pyz^{\bullet-}$ radicals, a through-space direct exchange interaction mechanism may be responsible for the low observed χT product. Broken-symmetry DFT calculations of a $(pyz^{\bullet-})_2$ fragment, extracted from the **Sm** crystal structure (170 K) without any subsequent geometry optimization, leads to a large energy stabilization of the singlet state relative to the triplet state by 0.11 eV, corresponding to a superexchange coupling constant of J/hc = −750 cm^{-1} (*cf.* Methods, Supplementary Fig. 7). This value of J largely exceeds that estimated from the Bonner-Fisher model. However, the proximity of the excited $^6H_{7/2}$ term by only ~1000 K, leads to experimentally determined room-temperature χT products being larger than predicted

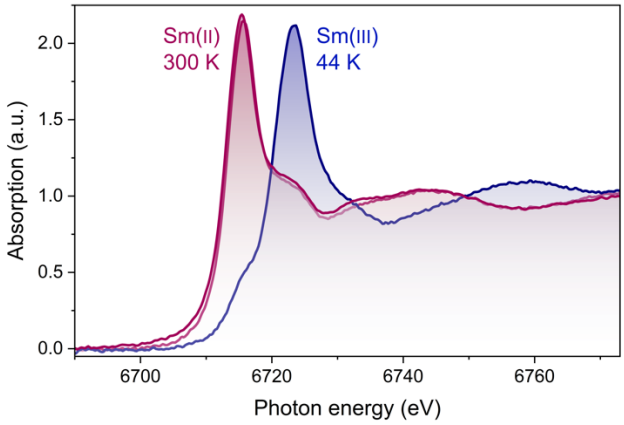

Fig. 3 | X-ray absorption spectroscopy. Sm L_3 XANES spectra of polycrystalline **Sm** measured at 300 K, at 44 K, and again at 300 K.

by the Curie constant for Sm(III).[41] In this perspective, the superexchange coupling constant originating from the Bonner-Fisher model may be significantly underestimated.

The reversibility of the VT transition in **Sm** is confirmed by successive cooling-heating cycles (Fig. 2b) where only a minor decrease and increase in $T_c\downarrow$ (of 3 K) and $T_c\uparrow$ (of 1 K), respectively, are observed after thirteen cycles. Increasing the temperature sweep rate up to 8 K min^{-1} leads to a gradual widening of the hysteresis loop (Fig. 2c) maximizing at $T_c\uparrow - T_c\downarrow$ = 28 K. Despite the rapid cycling, the powder X-ray diffractograms of the same sample before and after completion of 30 cycles with cooling and heating rates up to 8 K min^{-1} are virtually identical with a slight broadening setting in at the higher 2θ angles (Supplementary Fig. 8).

Solid solutions

In SmS, the doping of trivalent lanthanide ions allows for thermally induced VT transitions at ambient pressures.[42] This observation reflects a significant sensitivity of the VT transition to the chemical surroundings. Whilst initially believed to be driven entirely by chemical pressure induced by the smaller *Ln*(III) ions, the doping of *Ln*(II) ions smaller than Sm(II), such as Yb(II), was insufficient to induce VT transitions at ambient pressure. This result suggests that other factors, such as the dopant Ln(III) electronic structure, are key.[43] The room-temperature isomorphism of **Sm** and **Yb** allows for the doping of Yb(II) into **Sm**, utilizing a mixture of YbI_2 (10–50%) and SmI_2 (*cf.* Methods). Room-temperature powder X-ray diffraction experiments and Rietveld refinements suggest the formation of a single crystalline phase, $Sm_{1-x}Yb_xI_2(pyz)_3$ (denoted **Sm-Yb**(x)). For all x, **Sm-Yb**(x) is isomorphous to the high-temperature phase of **Sm**, with decreasing unit cell volumes for increasing Yb(II) concentration (*cf.* Supplementary Table 2 and Supplementary Fig. 9). The unit cell b length reflects the contraction along the ladder direction and decreases steadily with increasing Yb(II) concentration, as approximated by Vegard's law (Supplementary Fig. 10). The high-temperature part of the χT product for **Sm-Yb**(0.1) (Fig. 4) superimposes with the data for **Sm**, suggesting that no VT transition has been induced by the doping of 10% Yb(II). At lower temperatures, however, **Sm-Yb**(0.1) remains in the Sm(II) state before the χT product experiences a drop at $T_c\downarrow$ = 163 K, 29 K lower than for **Sm**. The effective size of Yb(II) in **Yb** (120 K) is slightly smaller than that of Sm(II) in **Sm** (230 K), as evidenced by the difference in average *Ln*—I and *Ln*—N bond lengths of 3.4% and 3.9%, respectively. On the contrary, the Yb(II) possesses longer average *Ln*—I and *Ln*—N bond lengths than the Sm(III) in **Sm** (170 K) of 0.3% and 2.9%, respectively, reflecting Yb(II) being effectively larger than Sm(III). The shift of T_c towards lower temperatures upon Yb(II)-doping suggests that the negative pressure induced by r(Yb(II)) > r(Sm(III)) in the low-temperature phase dominates over the positive pressure resulting from r(Yb(II)) < r(Sm(II)) in the high temperature phase. Upon further cooling to 3 K, the χT product coincides with the data for **Sm**, suggesting the presence of strongly coupled radical spins in **Sm-Yb**(0.1). Reheating leads to a full recovery of the high-temperature phase with a thermal hysteresis of 7 K, significantly smaller than that of **Sm** (14 K). Analogous experiments on **Sm-Yb**(x) with x up to 0.5 leads to a steady shift of the T_c to lower temperatures, a softening of the transition, and the gradual narrowing of the hysteresis loop, which closes for x = 0.3. For x = 0.3 and above, the low-temperature χT products show significant departures from the Bonner-Fisher model calculation suggesting an increasing concentration of uncompensated radical spins. Empirically, the T_c scales approximately linearly with x (Fig. 4, inset) suggesting that VT transition T_cs can be synthetically tailored anywhere between ~50 K and ~200 K in the **Sm-Yb**(x) molecule-based alloys.

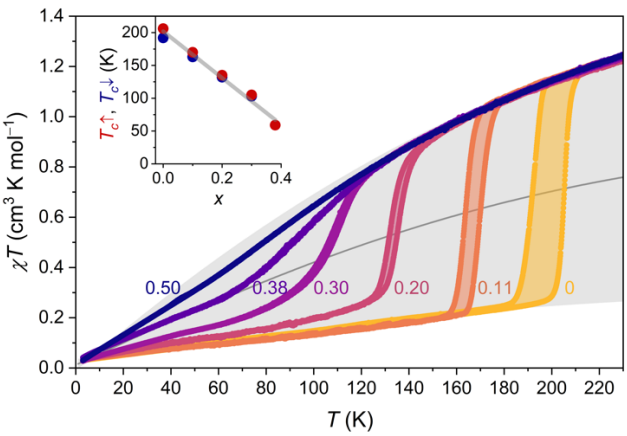

Fig. 4 | Magnetic properties of Sm-Yb(x) solid solutions. Magnetic susceptibility-temperature product, χT ($\mu_0 H$ = 1.0 T, temperature ramping rate = 0.25 K min^{-1}) of **Sm-Yb**(x) solid solutions, normalized to the Sm content, 1 – x. The grey surface represents the area spanned by the expected χT product for zero- and full conversion, as given by the data of Fig. 2a. The solid black line represents the 50%-molar fraction of the Sm(III) ⇄ Sm(II) conversion. The inset shows the temperature dependence of the T_cs *vs* x, with the best linear fit (grey line, T_c (K) = −3.55x + 202).

Outlook

Valence tautomerism in inorganic lanthanide-based materials is linked to dramatic changes in the material's physical properties. Despite being intensively pursued, analogous transitions in molecule-based lanthanide compounds remain almost non-existent.[44] In addition to the sole prior example of lanthanide-centered VT in a dinuclear Yb complex,[21] Ce- and Yb-based systems have been reported to exhibit intermediate valence.[45,46] Herein, we have demonstrated a complete, hysteretic, and fully reversible VT transition in a simple molecule-based lanthanide compound, $SmI_2(pyrazine)_3$. The extreme rarity of VT transitions in molecular lanthanide materials may be linked to the limited access to divalent (or tetravalent) lanthanide building blocks, although these have recently experienced a dramatic evolution and attracted significant attention. Considering just SmI_2 and YbI_2, research in the field of organic synthesis has elucidated the immense tunability of the *Ln*(III)/*Ln*(II) reduction potential targeted at specific chemical conversions. Furthermore, the reducing ability of LnI_2 is known to be tunable by light excitation.[47] We hypothesize that an analogous tunability could exist in the solid state and hosts the possibility for realizing materials displaying temperature-, pressure-, and light-driven *Ln*(III)/*Ln*(II) VT transitions. Here, polymeric materials such as metal-organic frameworks are of particular interest for engineering cooperativity and band structures. The itinerant electrons, found in the lanthanide(-based) metals, coexisting with the localized *f* electrons, could be realized in coordination polymers by metal-ligand orbital energy alignment, as demonstrated for the 3*d* transition elements. Such correlated phenomena, combined with a chemically encoded VT switch, would be unparalleled in any material.

References

1. Bünzli, J.-C. G. "Applications of Rare Earths" in *The Lanthanides and Actinides*, World Scientific (Liddle, S. T., Mills, D. P. & Natrajan, L. S.) pp. 633–685 (2022).
2. Ramanathan, A. et al. Chemical design of electronic and magnetic energy scales of tetravalent praseodymium materials. *Nat. Commun.* **14**, 3134 (2023).
3. Münzfeld, L. et al. Synthesis and properties of cyclic sandwich compounds. *Nature* (2023) DOI: 10.1038/s41586-023-06192-4.
4. Gould, C. A. et al. Ultrahard magnetism from mixed-valence dilanthanide complexes with metal-metal bonding. *Science* **375**, 198–202 (2022).
5. Sato, O. Dynamic molecular crystals with switchable physical properties. *Nat. Chem.* **8**, 644–656 (2016).
6. Tricoire, M., Mahieu, N., Simler, T. & Nocton, G. Intermediate Valence States in Lanthanide Compounds. *Chem. Eur. J.* **27**, 6860–6879 (2021).
7. Chen, B. et al. Novel Valence Transition in Elemental Metal Europium around 80 GPa. *Phys. Rev. Lett.* **129**, 016401 (2022).
8. Song, J., Fabbris, G., Bi, W., Haskel, D. & Schilling, J. S. Pressure-Induced Superconductivity in Elemental Ytterbium Metal. *Phys. Rev. Lett.* **121**, 037004 (2018).
9. Jayaraman, A., Narayanamurti, V., Bucher, E. & Maines, R. G. Continuous and Discontinuous Semiconductor-Metal Transition in Samarium Monochalcogenides Under Pressure. *Phys. Rev. Lett.* **25**, 1430 (1970).
10. Stevens, K. W. H. Fluctuating valence in SmS. *J. Phys. C: Solid State Phys.* **9**, 1417–1429 (1976).
11. Sousanis, A., Smet, P. F. & Poelman, D. Samarium Monosulfide (SmS): Reviewing Properties and Applications. *Materials* **10**, 953 (2017).
12. Haga, Y., Derr, J., Barla, A., Salce, B., Lapertot, G., Sheikin, I., Matsubayashi, K., Sato, N. K. & Flouquet. Pressure-induced magnetic phase transition in gold-phase SmS. *Phys. Rev. B* **70**, 220506(R) (2004).
13. Gilbert Corder, S. N. et al. Near-field spectroscopic investigation of dual-band heavy fermion metamaterials. *Nat. Commun.* **8**, 2262 (2017).
14. Stern, A., Dzero, M., Galitski, V. M., Fisk, Z. & Xia, J. Surface-dominated conduction up to 240 K in the Kondo insulator SmB_6 under strain. *Nat. Mater.* **16,** 708–712 (2017).
15. Robinson, P. J. et al. Dynamical Bonding Driving Mixed Valency in a Metal Boride. *Angew. Chem. Int. Ed.* **59**, 10996–11002 (2020).
16. Radzieowski, M., Stegemann, F., Block, T., Stahl, J., Johrendt, D. & Janka, O. Abrupt Europium Valence Change in $Eu_2Pt_6Al_{15}$ around 45 K. *J. Am. Chem. Soc.* **140**, 8950–8957 (2018).
17. Arvanitidis, J., Papagelis, K., Margadonna, S., Prassides, K. & Fitch, A. N. Temperature-induced valence transition and associated lattice collapse in samarium fulleride. *Nature* **425**, 599–602 (2003).
18. Buchanan, R. M. & Pierpont, C. G. Tautomeric catecholate-semiquinone interconversion via metal-ligand electron transfer. Structural, spectral, and magnetic properties of (3,5-di-*tert*-butylcatecholato)-(3,5-di-*tert*-butylsemiquinone)-(bipyridyl)cobalt(III), a complex containing mixed-valence organic ligands. *J. Am. Chem. Soc.* **102**, 4951–4957 (1980).
19. Hendrickson, D. N. & Pierpont, C. G. Valence Tautomeric Transition Metal Complexes. *Top. Curr. Chem.* **234**, 63–95 (2004).
20. Gransbury, G. K. & Boskovic, C. "Valence Tautomerism in d-block complexes" in *Encyclopedia of Inorganic and Bioinorganic Chemistry*, John Wiley & Sons, Ltd., pp. 1–24, Wiley (2021).
21. Fedushkin, I. L., Maslova, O. V., Morozov, A. G., Dechert, S., Demeshko, S. & Meyer, F. Genuine Redox Isomerism in a Rare-Earth-Metal Complex. *Angew. Chem. Int. Ed.* **51**, 10584–10587 (2012).
22. Fedushkin, I. L., Maslova, O. V., Baranov, E. V. & Shavyrin, A. S. Redox Isomerism in the Lanthanide Complex [(dpp-Bian)Yb(DME)(μ-Br)]$_2$ (dpp-Bian = 1,2-Bis[(2,6-diisopropylphenyl)imino]acenaphthene). *Inorg. Chem.* **48**, 2355–2357 (2009).
23. Pedersen, K. S. et al. Formation of the layered conductive magnet $CrCl_2(pyrazine)_2$ through redox-active coordination chemistry. *Nat. Chem.* **10**, 1056–1061 (2018).
24. Perlepe, P. et al. Metal-organic magnets with large coercivity and ordering temperatures up to 242°C. *Science* **370**, 587–592 (2020).
25. Huang, Y., Zhang, Q., Li, Y. C., Yao, Y., Hu, Y. & Ren, S. Chemical Tuning Meets 2D Molecular Magnets. *Adv. Mater.* **35**, 2208919 (2023).
26. Huang, Y. et al. Pressure-controlled magnetism in 2D molecular layers. *Nat. Commun.* **14**, 3186 (2023).

27. Perlepe, P. et al. From an antiferromagnetic insulator to a strongly correlated metal in square-lattice $MCl_2(pyrazine)_2$ coordination solids. *Nat. Commun.* **13**, 5766 (2022).
28. Voigt, L., Kubus, M. & Pedersen, K. S. Chemical engineering of quasicrystal approximants in lanthanide-based coordination solids. *Nat. Commun.* **11**, 4705 (2020).
29. Chen, H., Voigt, L., Kubus, M., Mihrin, D., Mossin, S., Larsen, R. W., Kegnæs, S., Piligkos, S. & Pedersen, K. S. Magnetic Archimedean Tessellations in Metal–Organic Frameworks. *J. Am. Chem. Soc.* **143**, 14041–14045 (2021).
30. Chen, H. et al. Towards frustration in Eu(II) Archimedean tessellations. *Chem. Commun.* **59**, 1609–1612 (2023).
31. Bratsch, S. G. Standard Electrode Potentials and Temperature Coefficients in Water at 298.15 K. *J. Phys. Chem. Ref. Data* **18**, 1–21 (1989).
32. Szostak, M., Fazakerley, N. J., Parmar, D. & Procter, D. J. Cross-Coupling Reactions Using Samarium(II) Iodide. *Chem. Rev.* **114**, 5959–6039 (2014).
33. Kubus, M., Voigt, L. & Pedersen, K. S. Pentagonal-bipyramidal acetonitrile complexes of the lanthanide(II) iodides. *Inorg. Chem. Commun.* **114**, 107819 (2020).
34. Kaim, W. The Versatile Chemistry of 1,4-Diazines: Organic, Inorganic and Biochemical Aspects. *Angew. Chem. Int. Ed.* **22**, 171–190 (1983).
35. Here, T_c is defined as the temperature at which Sm(III) and Sm(II) are present in equal amounts.
36. Fieser, M. E. et al. Evaluating the electronic structure of formal Ln^{II} ions in $Ln^{II}(C_5H_4SiMe_3)_3^{1-}$ using XANES spectroscopy and DFT calculations. *Chem. Sci.* **8**, 6076–6091 (2017).
37. Deen, P.P., Braithwaite, D., Kernavanois, N., Paolasini, L., Raymond, S., Barla, A., Lapertot, G. & Sanchez, J.P. Structural and electronic transitions in the low-temperature, high-pressure phase of SmS. *Phys. Rev. B* **71**, 245118 (2005).
38. Zasimov, P., Amidani, L., Retegan, M., Walter, O., Caciuffo, R. & Kvashnina, K. O. HERFD-XANES and RIXS Study on the Electronic Structure of Trivalent Lanthanides across a Series of Isostructural Compounds. *Inorg. Chem.* **61**, 1817–1830 (2022).
39. Fatila, E. M., Maahs, A. C., Mills, M. B., Rouzières, M., Soldatov, D. V., Clérac, R. & Preuss, K. E. Ferromagnetic ordering of –[Sm(III)-radical]$_n$– coordination polymers. *Chem. Commun.* **52**, 5414–5417 (2016).
40. Bonner, J. C. & Fisher, M. E. Linear Magnetic Chains with Anisotropic Coupling. *Phys. Rev.* **135**, A640 (1964).
41. Pan, Y.-Z., Hua, Q.-Y., Lin, L.-S., Qiu, Y.-B., Liu, J.-L., Zhou, A.-J., Lin, W.-Q. & Leng, J.-D. A slowly magnetic relaxing Sm^{III} monomer with a D_{5h} equatorial compressed ligand field. *Inorg. Chem. Front.* **7**, 2335–2342 (2020).
42. Jayaraman, A., Bucher, E., Dernier, P. D. & Longinotti, L. D. Temperature-Induced Explosive First-Order Electronic Phase Transition in Gd-Doped SmS. *Phys. Rev. Lett.* **31**, 700–703 (1973).
43. Jayaraman, A. & Maines, R. G. Study of the valence transition in Eu-, Yb-, and Ca-substituted SmS under high pressure and some comments on other substitutions. *Phys. Rev. B* **19**, 4154–4161 (1979).
44. Hay, M. A. & Boskovic, C. Lanthanoid Complexes as Molecular Materials: The Redox Approach. *Chem. Eur. J.* **27**, 3608–3637 (2021).
45. Walter, M. C., Booth, C. H., Lukes, W. W. & Andersen, R. A. Cerocene Revisited: The Electronic Structure of and Interconversion Between $Ce_2(C_8H_8)_3$ and $Ce(C_8H_8)_2$. *Organometallics* **28**, 698–707 (2009).
46. Booth, C. W. et al. Intermediate-Valence Tautomerism in Decamethylytterbocene Complexes of Methyl-Substituted Bipyridines. *J. Am. Chem. Soc.* **49**, 17537–17549 (2010).
47. Sumino, Y., Harato, N., Tomisaka, Y. & Ogawa, A. A novel photoinduced reduction system of low-valent samarium species: reduction of organic halides and chalcogenides, and its application to carbonylation with carbon monoxide. *Tetrahedron* **59**, 10499–10508 (2003).

Methods

General methods

All manipulations were performed inside an Ar-filled glovebox (Inert I-Lab, O_2 <0.1 ppm, H_2O <0.5 ppm). Solvents were dried using an Inert solvent purification system and stored over 0.3 Å molecular sieves. SmI_2 (>99.99%, Thermo Fisher Scientific), YbI_2 (>99%, Alfa Chemistry), and pyrazine (>99%, Sigma-Aldrich) were used as received. Elemental analysis of Sm, Yb, C, H, and N were performed by Mikroanalytisches Laboratorium Kolbe (Fraunhofer Institut UMSICHT, Oberhausen, Germany).

Synthesis of $SmI_2(pyz)_3$ (Sm) and $YbI_2(pyz)_3$ (Yb)

A warm solution of LnI_2 (*Ln* = Sm: 100 mg, 0.25 mmol; *Ln* = Yb: 100 mg, 0.23 mmol) in acetonitrile (2.5 mL) was added to a melt (60 °C) of pyrazine (800 mg, 10 mmol), yielding almost immediate precipitation of solid. The mixture was cooled slowly to room temperature, isolated by vacuum filtration, washed with diethyl ether (3 × 3 mL) and dried, yielding a microcrystalline, dark blue-grey solid. Yield: 100 mg (65%) for **Sm** and 130 mg (84%) for **Yb**. Anal. calcd (found) for **Sm**: C, 22.37% (21.82%), H, 1.88% (1.90%), N, 13.04% (12.91%). Anal. calcd (found) for **Yb**: C, 21.60% (21.26%), H, 1.81% (1.78%), N, 12.60% (12.37%).

Synthesis of $Sm_{1-x}Yb_xI_2(pyz)_3$ (Sm-Yb(*x*))

The **Sm-Yb** solid solutions were prepared analogously using the following ratios of LnI_2:

Sm-Yb(0.1): YbI_2 (10.5 mg, 0.025 mmol), SmI_2 (89.8 mg, 0.222 mmol). Yield: 84%. *x* found: 0.11.

Sm-Yb(0.2): YbI_2 (21.0 mg, 0.049 mmol), SmI_2 (76.6 mg, 0.190 mmol). Yield: 82%. *x* found: 0.20.

Sm-Yb(0.3): YbI_2 (31.7 mg, 0.074 mmol), SmI_2 (69.0 mg, 0.170 mmol). Yield: 83%. *x* found: 0.30.

Sm-Yb(0.4): YbI_2 (42.2 mg, 0.099 mmol), SmI_2 (60.0 mg, 0.148 mmol). Yield: 87%. *x* found: 0.38.

Sm-Yb(0.5): YbI_2 (49.7 mg, 0.12 mmol), SmI_2 (50.6 mg, 0.125 mmol). Yield: 81%. *x* found: 0.50.

X-ray diffraction and crystallography

Single crystal X-ray diffraction was collected on an Oxford Diffraction Supernova single crystal diffractometer, with an Atlas CCD detector. Crystals were obtained directly from the reaction solutions, covered in polybutene oil in a glovebox and mounted on nylon loops for measurement. A single crystal of **Sm** was measured with Mo Kα radiation (λ = 0.71073 Å) at 230 and 170 K (cooling rate of 0.5 K min^{-1}). A single crystal of **Yb** was measured with Cu Kα radiation

(λ = 1.5406 Å) at 120 K. Single crystal X-ray diffraction data were reduced using CrysAlisPro[48] and corrected using a numerical absorption correction based on Gaussian integration over a multi-faceted crystal model. All structures were solved with the SHELXS[49] structure solution program using direct methods and refined with the SHELXL[50] refinement package using least squares minimisation on all data, in Olex2.[51] All non-hydrogen atoms were refined anisotropically, with hydrogen atoms placed at geometrical estimates and refined using the riding model. For **Sm**, the pendant pyz (*iii*) is disordered over a plane of symmetry, and was refined with rigid bond restraints and similar thermal displacement parameters for neighboring atoms at both temperatures.

Powder X-ray diffraction data were obtained using Cu Kα radiation (λ = 1.5406 Å) in sealed borosilicate glass capillaries (∅ 0.5 mm). Powder X-ray diffraction data were obtained for all compounds at room temperature on a Malvern Panalytical Empyrean powder X-ray diffractometer equipped with a 1Der detector. Variable temperature powder X-ray diffraction data for **Sm** were obtained on an Oxford Diffraction Supernova single crystal diffractometer, equipped with an Atlas CCD detector. Data were obtained on a single capillary, upon cooling and subsequent heating. Data were obtained with a cooling and heating rate of 0.5 K min^{-1} to maintain crystallinity, and the sample was allowed to thermally equilibrate for 5 min at each temperature.

Rietveld refinements were performed in the HighScore Plus 5.1.0 program suite.[52] All structures were refined against the **Sm** (230 K) crystal structure and the peak profiles were fit using a pseudo-Voigt function. All atomic positions were kept fixed, and the occupancy fixed to the specific Sm:Yb ratios.

Magnetization measurements

The magnetization data were obtained using a QuantumDesign Dynacool Physical Property Measurement System (PPMS) and the vibrating sample magnetometer (VSM) option. The temperature of magnetic field windows of 2 K to 300 K, and −9 to +9 T. The temperature sweeping rates were kept between 0.25 K min^{-1} and 6 K min^{-1}. The samples (9–13 mg) were loaded into standard QuantumDesign PTFE powder capsules, sealed with PTFE-tape and quickly moved to the PPMS chamber. The data were corrected for diamagnetic contributions from the sample and the sample environment.

X-ray absorption spectroscopy

X-ray absorption near edge spectroscopy (XANES) data at the Sm L_3 edge were acquired at the ID12 beamline (ESRF – The European Synchrotron, Grenoble, France). The sample was enclosed in a flame-sealed quartz capillary (∅ 0.9 mm). The data collected at 44 K and room temperature were recorded using total fluorescence yield detection mode and were not corrected for re-absorption effect. The intensity of the incident X-ray beam was carefully adjusted to avoid radiation damage of the sample. For the sake of comparison, the spectra were normalized using standard procedures.

DFT calculations

Density functional theory calculations were performed with the ORCA programme suite using the atomic coordinates determined by single-crystal X-ray crystallography (T = 170 K) without any subsequent geometry optimization.[53] The calculations employed the TPSSh functional together with the SARC (scalar-relativistically contracted) version of the ZORA-def2-TZVP basis set with the corresponding auxiliary basis.[54,55,56,57] Superexchange coupling constants were obtained using the broken-symmetry method and the approach of Yamaguchi.[58,59]

Data availability

Crystallographic data for the structures reported in this article have been deposited at the Cambridge Crystallographic Data Centre, under deposition numbers CCDC 2285789 (**Sm** at 230 K), 2285788 (**Sm** at 170 K), and 2285790 (**Yb** at 120 K). Copies of the data can be obtained free of charge via https://www.ccdc.cam.ac.uk/structures/.

References

48. Agilent (2014). CrysalisPro. Agilent Technologies Ltd, Oxfordshire, England.
49. Sheldrick, G. M. A short history of SHELX. *Acta Crystallogr. A*, **64**, 112–122 (2008).
50. Sheldrick, G. M. Crystal structure refinement with SHELXL. *Acta Crystallogr. C*, **71**, 3–8 (2015).
51. Dolomanov, O.V., Bourhis, L. J., Gildea, R.J, Howard, J.A.K. & Puschmann, H. OLEX2: a complete structure solution, refinement and analysis program. *J. Appl. Cryst.* **42**, 339-341 (2009).
52. Degen, T., Sadki, M., Bron, E., König, U. & Nénert, G. The HighScore suite. *Powder Diffr.* **29**, S13–S18 (2014).
53. Neese, F. Software update: the ORCA program system, version 4.0. *WIREs Comput. Mol. Sci.* **8**, e1327 (2018).
54. Pantazis, D. A. & Neese, F. All-Electron Scalar Relativistic Basis Sets for the Lanthanides. *J. Chem. Theory Comput.* **5**, 2229–2238 (2009).
55. Rolfes, J. D., Neese, F. & Pantazis, D. A. All-electron scalar relativistic basis sets for the elements Rb—Xe. *J. Comput. Chem.* **41**, 1842—1849 (2020).
56. F. Weigend. Accurate Coulomb-fitting basis sets for H to Rn. *Phys. Chem. Chem. Phys.* **8**, 1057—1065 (2006).
57. Pantazis, D. A. & Neese, F. All-electron scalar relativistic basis sets for the 6*p* elements. *Theor. Chem. Acc.* **131**, 1292 (2012).
58. Yamaguchi, K., Takahara, Y. & Fueno, T. "Ab-Initio Molecular Orbital Studies of Structure and Reactivity of Transition Metal-Oxo Compounds" in *Applied Quantum Chemistry*; Smith, V. H., Schaefer, H. F. & Morokuma, K. (Eds.), D. Reidel: Boston, 155—184 (1986).
59. Yamanaka, S., Kawakami, T., Nagao, H. & Yamaguchi, K. Effective exchange integrals for open-shell species by density functional methods. *Chem. Phys. Lett.* **231**, 25—33 (1994).

Acknowledgements

K.S.P. thanks the VILLUM Foundation for a VILLUM Young Investigator+ (42094) grant, the Independent Research Fund Denmark for a DFF-Sapere Aude Starting Grant (0165-00073B), and the Carlsberg Foundation for a research infrastructure grant (CF17-0637). The X-ray spectroscopy experiments were performed at the ID12 beamline at the European Synchrotron Radiation Facility (ESRF, Grenoble, France). We thank the Danish Agency for Science, Technology, and Innovation for funding the instrument center Danscatt.

Author contributions

K.S.P. and M.A.D. conceived and planned the research project. M.A.D., F.A., and A.S.M. developed and performed the synthesis and the crystallographic analysis. M.A.D., K.S.P., and J.B. performed the characterization of the magnetic properties. N.Y. and A.R. acquired and analysed the X-ray spectroscopic data. J.B. performed the DFT calculations. The manuscript was written by K.S.P. and M.A.D. with input from all coauthors. All authors have given their consent to the publication of the manuscript.

Competing interests

The authors declare no competing interests.